Available online at www.sciencedirect.com
SCIENCE DIRECT®
ELSEVIER
Nuclear Instruments and Methods in Physics Research A 524 (2004) 102–114
NUCLEAR INSTRUMENTS & METHODS IN PHYSICS RESEARCH Section A
www.elsevier.com/locate/nima

# Measurement of the n_TOF beam profile with a micromegas detector

J. Pancin[a,*], U. Abbondanno[b], G. Aerts[a], H. Alvarez[c], S. Andriamonje[a], A. Angelopoulos[d], P. Assimakopoulos[e], C. Bacri[f], G. Badurek[g], P. Baumann[h], F. Bečvář[i], H. Beer[j], J. Benlliure[c], B. Berthier[f], E. Berthoumieux[a], S. Boffi[k], C. Borcea[l], E. Boscolo-Marchi[m], N. Bustreo[m], F. Calvino[n], D. Cano-ott[o], R. Capote[p], P. Carlson[q], P. Cennini[l], V. Chepel[r], E. Chiaveri[l], N. Colonna[s], G. Cortes[n], D. Cortina[c], A. Couture[t], J. Cox[t], S. Dababneh[j], M. Dahlfors[l], S. David[f], A. Delbart[a], J. Derre[a], R. Dolfini[k], C. Domingo[u], I. Duran-Escribano[c], C. Eleftheriadis[v], M. Embid-Segura[o], L. Ferrant[f], A. Ferrari[l], L. Ferreira-Lourenco[w], R. Ferreiramarques[r], H. Frais-Koelbl[x], W. Furman[y], Y. Giomataris[a], I. Goncalves[w], E. Gonzalez-Romero[o], A. Goverdovski[z], F. Gramegna[m], E. Griesmayer[x], F. Gunsing[a], R. Haight[aa], M. Heil[j], A. Herrera-Martinez[l], K. Ioannides[e], N. Janeva[ab], F. Jeanneau[a], E. Jericha[g], F. Käppeler[j], Y. Kadi[l], D. Karamanis[e], A. Kelic[h], V. Ketlerov[z], G. Kitis[v], P. Koehler[ac], V. Konovalov[y], E. Kossionides[ad], V. Lacoste[l], H. Leeb[g], A. Lindote[r], I. Lopes[r], M. Lozano[p], S. Lukic[h], S. Markov[ab], S. Marrone[s], J. Martinez-Val[ae], P. Mastinu[m], A. Mengoni[l], P. Milazzo[b], E. Minguez[ae], A. Molina-Coballes[p], C. Moreau[f], F. Neves[r], H. Oberhummer[g], S. O'brien[t], I. Papadopoulos[l], T. Papavengelou[v], C. Paradela[c], A. Pavlik[af], P. Pavlopoulos[ag], A. Perez-Parra[o], J. Perlado[ae], V. Peskov[q], L. Perrot[a], V. Peskov[q], R. Plag[j], A. Plompen[ah], A. Plukis[a], A. Poch[n], A. Policarpo[r], C. Pretel[n], J. Quesada[p], M. Radici[k], S. Raman[ac], W. Rapp[j], R. Reifarth[j], F. Rejmund[f], M. Rosetti[ai], C. Rubbia[k], G. Rudolf[h], P. Rullhusen[ah], J. Salgado[w], E. Savvidis[v], C. Stephan[f], G. Tagliente[s], J. Tain[u], C. Tapia[n], L. Tassan-Got[f], L. Tavora[w], R. Terlizzi[s], M. Terrani[k], N. Tsangas[aj], G. Vannini[b], P. Vaz[w], A. Ventura[ai], D. Villamarin-Fernandez[o], M. Vincente-Vincente[o], V. Vlachoudis[l], R. Vlastou[ak], F. Voss[j], H. Wendler[l], M. Wiescher[t], K. Wisshak[j], L. Zanini[l]

[a] *CEA/Saclay - DSM, DAPNIA/SphN, Orme des Merisiers Bat 703/37C, F-91191 Gif-sur-Yvette, France*
[b] *Instituto Nazionale di Fisica Nuclear-Trieste, Italy*
[c] *Universidade de Santiago de Compostela, Spain*

*Corresponding author. Tel.: +33-1-69-08-75-02; fax: +33-1-69-08-75-84.
*E-mail address:* jpancin@cea.fr (J. Pancin).


doi:10.1016/j.nima.2004.01.055

[d] Astro-Particle Consortium, Nuclear Physics Lab., University of Athens, Greece
[e] Astro-Particle Consortium, Nuclear Physics Lab., University of Ioannina, Greece
[f] Centre National de la Recherche Scientifique/IN2P3 - IPN, Orsay, France
[g] Atominstitut der Österreichischen Universitäten,Technische Universität Wien, Austria
[h] Centre National de la Recherche Scientifique/IN2P3 - IreS, Strasbourg, France
[i] Charles University, Prague, Czech Republic
[j] Forschungszentrum Karlsruhe GmbH (FZK), Institut für Kernphysik, Germany
[k] Universita degli Studi Pavia, Pavia, Italy
[l] CERN, Geneva, Switzerland
[m] Laboratori Nazionali di Legnaro, Italy
[n] Universitat Politecnica de Catalunya, Barcelona, Spain
[o] Centro de Investigaciones Energeticas Medioambientales y Technologicas, Madrid, Spain
[p] Universidad de Sevilla, Spain
[q] Kungliga Tekniska Hogskolan, Physics Department, Stockholm, Sweden
[r] Laboratorio de Instrumentacao e Phisica Experimental de Particulas - Coimbra & Departamento de Fisica da Universidade de Coimbra, Portugal
[s] Instituto Nazionale di Fisica Nuclear-Bari, Italy
[t] University of Notre Dame, Notre Dame, USA
[u] Consejo Superior de Investigaciones Cientificas, University of Valencia, Spain
[v] Astro-Particle Consortium,Nuclear Physics Lab., University of Thessaloniki, Greece
[w] Instituto Tecnológico e Nuclear, Lisbon, Portugal
[x] Fachhochschule Wiener Neustadt, Wiener Neustadt, Austria
[y] Joint Institute for Nuclear Research, Frank Laboratory of Neutron Physics, Dubna, Russia
[z] Institute of Physics and Power Engineering, Kaluga region, Obninsk, Russia
[aa] Los Alamos National Laboratory, NM, USA
[ab] Institute for Nuclear Research and Nuclear Energy, Sofia, Bulgaria
[ac] Oak Ridge National Laboratory, Physics Division, Oak Ridge, USA
[ad] Astro-Particle Consortium, Nuclear Physics Institute, NCSR "Demokritos", Athens, Greece
[ae] Universidad Politecnica de Madrid, Spain
[af] Institut für Isotopenforschung und Kernphysik, Universität Wien, Austria
[ag] Department of Physics and Astronomy - University of Basel, Basel, Switzerland
[ah] CEC-JRC-IRMM, Geel, Belgium
[ai] ENEA, Bologna, Italy
[aj] Astro-Particle Consortium,Nuclear Physics Dep., University of Thrace, Greece
[ak] Astro-Particle Consortium, Nuclear Physics Dep., Technical University of Athens, Greece

Received 11 August 2003; received in revised form 6 January 2004; accepted 8 January 2004

**Abstract**

A Micromegas detector was used in the neutron Time-Of-Flight (n_TOF) facility at CERN to evaluate the spatial distribution of the neutron beam as a function of its kinetic energy. This was achieved over a large range of neutron energies by using two complementary processes: at low energy by capture of a neutron via the $^{6}$Li$(n,\alpha)$t reaction, and at high energy by elastic scattering of neutrons on gas nuclei (argon + isobutane or helium + isobutane). Data are compared to Monte Carlo simulations and an analytic function fitting the beam profile has been calculated with a sufficient precision to use in neutron capture experiments at the n_TOF facility.


*PACS:* 29.40.Cs; 29.40.Gx; 29.27.fh; 28.20.−v

*Keywords:* n_TOF; Beam profile; Neutron beam profiler; Micromegas

## 1. Introduction

A new neutron Time-Of-Flight (n_TOF) facility is now operational at CERN [1,2]. This facility aims at measuring neutron-induced cross-sections essential for the design of Accelerator Driven System (ADS). This system is an innovative concept for energy production, incineration of nuclear waste and radioisotope production for medical applications [3–5]. Certain cross-section measurements are also of particular interest for astrophysics, notably for the explanation of the formation of heavy elements in our universe.

The n_TOF facility produces a high intensity flux of neutrons by the spallation process induced by 20 GeV protons onto a solid lead target surrounded by a water moderator. The pulsed proton beam has a maximum frequency of 0.8 Hz and the resultant neutron beam is cropped with two collimators that are placed between the experimental area and the spallation target. The first collimator is 2 m long with an inner radius of 5.5 cm and it is placed at 135.54 m from the target. The second collimator is 2.5 m long with an inner radius of 0.9 cm and placed at 175.35 m. The knowledge of the beam shape is of vital importance for the measurement of the cross-sections. In this article, we report the result obtained from an experiment where a new neutron detector based on the Micromegas concept [6–8] was placed at 186 m from the spallation target to evaluate the spatial characteristics of the n_TOF beam.

We present here a description of the detector, an analysis of the experimental data and a comparison with Monte Carlo simulations. Finally, we show how an analytic beam profile approximation can be obtained.

## 2. The Micromegas detector

### 2.1. Technical description

The Micromegas detector is composed of two chambers. The outer chamber constructed of aluminium is fixed to the n_TOF tube and the inner chamber, filled with the gas, is devoted to the detection (Fig. 1).

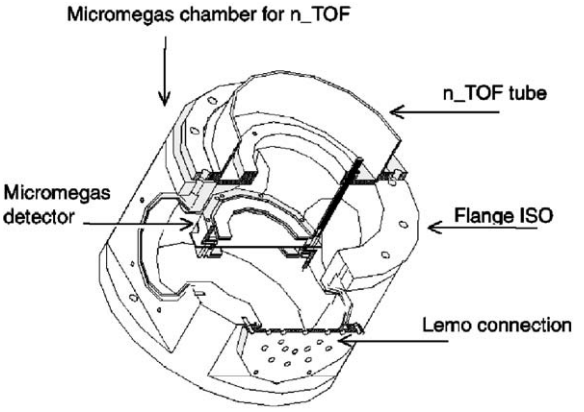


Fig. 1. Schematic view of the Micromegas chamber.

The inner chamber is a cylinder composed of two pieces of DELRIN with a diameter of 150 mm, closed at the ends by kapton foils of 75 μm thick and fixed to the DELRIN by two collars. The detector is filled with a mixture of argon–isobutane or helium–isobutane at atmospheric pressure. The kapton foils isolate the detector from the vacuum ($\simeq 10^{-3}$ mbar) [9].

The detector is a double-stage parallel plate circular chamber. It consists of a drift gap of 3 mm and an amplification gap of 100 μm. The two gaps are separated by a 5 μm thick nickel micromesh with square openings of 37 μm side every 50 μm. Amplification occurs between the mesh and a copper printed circuit with 50 strips of 1.5 mm wide spaced 100 μm apart. Thus, the detection area of the detector is a circle with a radius of 4 cm. Some spacers insulate the printed circuit form the micromesh and guarantee the uniformity of the amplification gap. The drift electrode covering all the detection area is a 20 μm thick aluminium foil on which a 500 nm layer of LiF made of pure $^{6}$Li has been deposited. The LiF layer is coated with 10 nm aluminium to avoid oxidation.

### 2.2. The detector principle

When charged particles travel through the gas, electrons are produced between the drift electrode and the micromesh by the ionization process. The applied electric field causes these electrons to drift

towards the micromesh. After crossing the 3 mm gap, they are multiplied in the narrow amplification gap (Fig. 2: with HV1 = 425 V and HV2 = 325 V in the argon mixture and HV1 = 725 V and HV2 = 325 V in the helium mixture). The subsequent electron avalanche induces a current on the anode strips. However, a neutron/charged particle converter is necessary to detect the incident n_TOF neutron beam. Since the useful neutron energy range of the n_TOF experiment extends from 0.1 eV to 250 MeV, there is no unique choice of converter over this wide energy range [10].

For low energies ($E_n < 10$ keV), the conversion reaction used is neutron capture on $^6$Li deposited on the entry face:

$$^6_3\mathrm{Li} + \mathrm{n} \rightarrow ^4_2\mathrm{He} + ^3_1\mathrm{H}, \quad Q = 4.78\ \mathrm{MeV}. \tag{1}$$

Provided the incoming neutron energy is negligible compared to the reaction Q value, the two reaction products (the alpha and the triton) are emitted in opposite directions with $E_t = 2.73$ MeV and $E_\alpha = 2.05$ MeV. This reaction has a cross-section of 940 barns at 25 meV (thermal neutrons), which decreases as $1/\sqrt{E}$ up to a neutron kinetic energy of about 50 keV and has a resonance at 240 keV [11].

At higher energies, the recoils of the gas nuclei are also detected [10]. The Micromegas detector is filled with He + $i$C$_4$H$_{10}$(3.8%) or Ar + $i$C$_4$H$_{10}$(2%). For safety reasons, the percentage of isobutane is low enough to have non-flammable gas. Above the threshold of detection, the recoil due to elastic scattering of a neutron on a gas nucleus is detectable in addition to the tritons and the alphas of the precedent reaction. The nucleus will be emitted around the forward direction with an energy distributed between 0 and $E_r(\theta_{lab} = 0)$ where

$$E_r(\theta_{lab}) = \frac{4A}{(A+1)^2}(\cos^2\theta_{lab})E_n \tag{2}$$

with $A$ the atomic mass of the recoil nucleus, $\theta_{lab}$ the angle between the recoil direction and the incoming neutron and $E_n$ the energy of the incoming neutron. The lighter the nucleus, the larger is the energy transfered from the incident neutron. The hydrogen nucleus is of particular interest since the recoil proton can absorb the complete neutron energy. Thus the isobutane is not only useful as a quench gas but also provides hydrogen to create proton recoils. In the case of the helium mixture, the helium recoils are also detected. Moreover, the reaction He(n,n)He has a resonance at 1 MeV which strongly increases the reaction rate (see Section 3.1).

### 2.3. Electronics and data acquisition system

The neutron energy is obtained by measuring its time of flight in the n_TOF tube. The time origin from which the detector begins to count is given by the impact of each proton bunch on the spallation

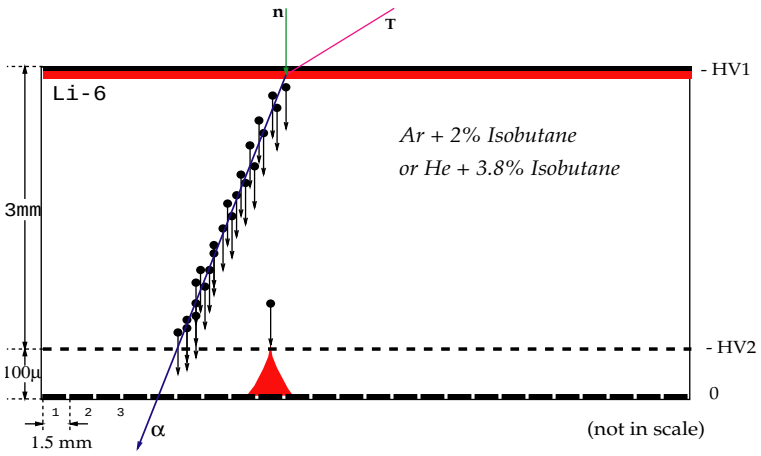


Fig. 2. Micromegas principle for neutron detection.

target. Fast electronics are needed to process the signal from the Micromegas strips. Each strip was connected to a fast current preamplifier[1] with about 1 ns of rise time. These preamplifiers are linked to 1 GHz flash ADCs.[2] A zero suppression is applied: signals above a given threshold are sampled and stored with a certain number of presamples and postsamples. This threshold was set at 5 mV in amplitude ($5.5 \times 10^5$ electrons ENC) for the argon mixture and 4.5 mV ($5 \times 10^5$ electrons ENC) for the helium mixture, corresponding to minimum deposited energies of 40 and 7 keV, respectively. The data were transfered by Gigabit links from the flash ADCs to the CDR (Central Data Recording facility at CERN) [12].

### 2.4. Detector efficiency

In Table 1 are presented the range and the energy deposit of the particles coming from absorption in LiF or elastic scattering in the helium mixture. To be detected, each particle has to deposit more than the threshold energy. The detection efficiency of the two gas mixtures is evaluated using a Monte Carlo simulation and the SRIM code (Stopping Ranges of Ions in Matter) [13]. The different processes of detection ($^6$Li absorption, proton, helium, carbon and argon recoils) are taken into account in the calculation. For each process, the reaction yield $Y_r$ is calculated as a function of the neutron energy

$$Y_r(E) = (1 - \exp(-N_a \sigma_t(E))) \frac{\sigma_r(E)}{\sigma_t(E)} \quad (3)$$

where $\sigma_r$ is the cross-section of the reaction, $\sigma_t$ the total cross-section and $N_a$ the number of atoms per square centimeters. The yield is then corrected for the efficiency of the different processes. For the $n(^6\mathrm{Li}, t)\alpha$ reaction, the tritons and alphas are detected with 100% efficiency since their energy deposits are above threshold (see Table 1). However, a small correction is applied to the alpha detection. In the simulation, the alpha particles are generated uniformly in the LiF deposit with an isotropic direction. Only 95% of them will exit from the drift electrode and deposit enough energy in the two gases. Concerning the recoil reactions, the recoils are generated uniformly in the drift gap and the angle is chosen using the differential cross-section given by ENDF [14]. All the recoils depositing less than the threshold are discarded form the calculation. The efficiencies are plotted for the two gases in Figs. 3 and 4.

Table 1
Maximal path and energy deposit in helium/isobutane (3.8%)

| Particle | Energy (keV) | Maximal path (mm) | Energy deposit in 3 mm (keV) |
|---|---|---|---|
| α | 2050 | 37 | 150 |
| $^3$H | 2730 | 463 | 15 |
| p recoil | 100 | 4.6 | 81 |
| p recoil | 500 | 27.9 | 40 |
| p recoil | 1000 | 82.4 | 23 |
| He recoil | 100 | 4.2 | 82 |
| He recoil | 500 | 11.2 | 200 |
| He recoil | 1000 | 18.4 | 190 |

## 3. Determination of the n_TOF beam profile

### 3.1. Data analysis

Data were taken during 1 week with a rate of 100 signals per proton pulse. The digitized signals were processed through an algorithm to identify each individual pulse. Five parameters were extracted from each pulse: the time of the start, peak and end, the pulse amplitude and the pulse area. In the analysis, it was considered that pulses on adjacent strips with a start time within a 200 ns time window formed a cluster and therefore corresponded to a single neutron interaction. Information for each cluster, the multiplicity (number of strips in the cluster), the total energy deposit (proportional to the total area), the mean amplitude and the time of flight of the incoming neutron were then extracted. The deposited energy and the strip multiplicity are directly linked to the type of the particle and its direction. For example, a particle parallel to the strips gives a low cluster size (see Fig. 5a) with a high energy deposited if it is parallel to the detector plane or a low deposit if

[1] From *Minicircuit* ref. ZFL-500LN.
[2] Acqiris DC240/DC270.

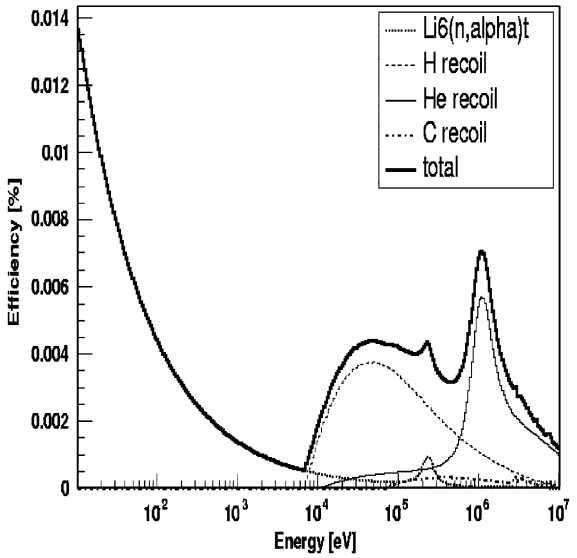


Fig. 3. Simulated detection efficiency in the helium mixture.

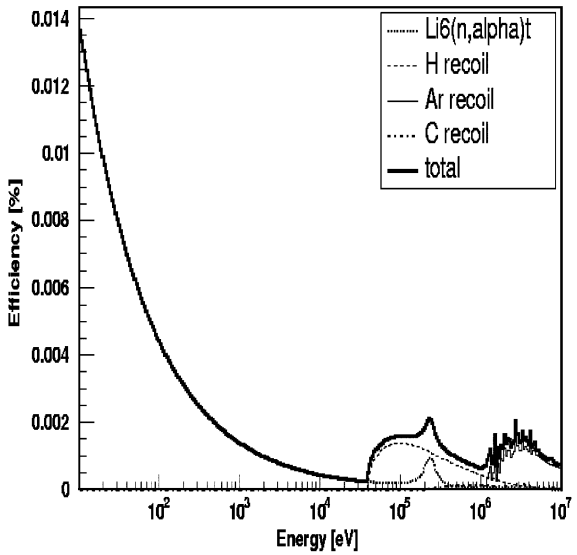


Fig. 4. Simulated detection efficiency in the argon mixture.

it is perpendicular. Conversely, a particle perpendicular to the strips and parallel to the entry face will give a high cluster size (see Fig. 5b) and a low energy deposited per strip. Since the time for a particle to cross the detector is negligible with respect to the drift time, the first pulse in the cluster corresponds to the electrons created near the micromesh while the last pulse, delayed by the electronic drift time in the 3 mm gap, corresponds to the electrons created close to the drift electrode. This drift time depends on the gas used and was about 150 ns for argon and 200 ns for helium. The strip of the last pulse in the cluster gives the position of the reaction and the start time of the first pulse gives the time of flight of the incident neutron. The former is used for the projected beam profile while the latter is used to study the reaction rate as a function of the neutron energy. The start time of each pulse is determined with a 10 ns accuracy. As a consequence, the accuracy on the time of flight is between 10 ns and the drift time in the gas. The simulation used to estimate the efficiency, permitted also to evaluate the time accuracy. The largest error found was 60 ns in the entire energy domain between 10 eV and 20 MeV with the helium mixture (45 ns in the argon mixture). It corresponds to an error on the energy of 4% at 20 MeV and 0.1% at 10 keV. The neutron kinetic energy is calculated using the time of flight and the distance (186 m) at which the detector is placed from the spallation target.

The reaction rate is the product of the cross-sections of the different reaction processes, the neutron flux, and the efficiency of the detector (Fig. 6). It clearly shows the $1/\sqrt{E}$ dependence of the neutron capture cross-section of $^{6}$Li and the main resonance at 240 keV. The $^{16}$O resonances at 0.433 and 1 MeV are due to the water placed around the target to cool it and to moderate the neutron flux to obtain a better energy resolution of the facility [5]. The evaporation peak of the neutron flux can be distinguished in the argon mixture but not in the He mixture since it coincides with the resonance of the neutron elastic scattering on He at 1 MeV. For energies above threshold (7 keV for helium and 40 keV for argon), a change in the slope of the reaction rate can be seen, which corresponds to the start of recoil detection.

### 3.2. The projected beam profiles

#### 3.2.1. Experimental profiles

The projected beam profile is the histogram of the neutron density per strip given by the

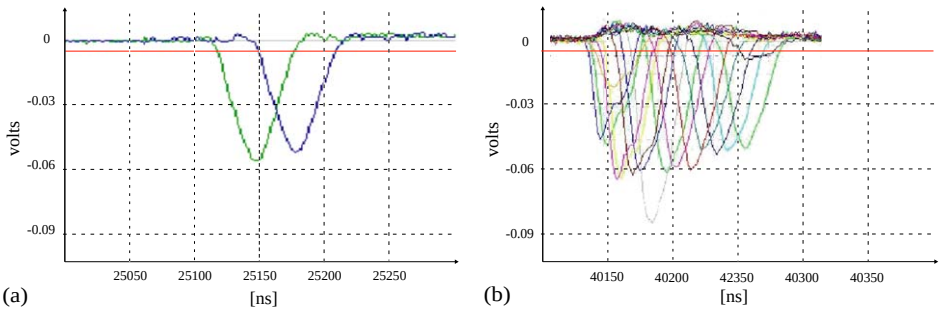


Fig. 5. Micromegas pulses induced by an alpha particle on contiguous strips with (a) low (b) high cluster size.

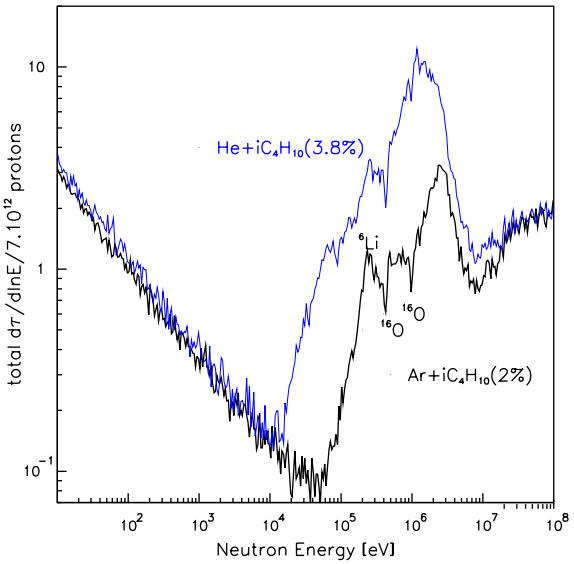


Fig. 6. Experimental reaction rate normalized to one bunch of $7 \times 10^{12}$ protons.

interaction position of each cluster. The time of flight measurement permits its extraction for various neutron energy ranges. It was considered that a low energy deposit in a cluster corresponded either to noise or to reactions leading to an insufficient ionization in the detector. In this case, the position of the reaction could not be found with a high confidence level and the event was not included in the histogram. Figs. 7a and b show the cluster area divided by the multiplicity in the argon mixture. The multiplicity is distributed between one and five from 10 eV to 40 keV and between one and three at higher energies but always peaked around one. At low energy in Fig. 7a, tritons deposit less energy than the alphas while at high energy it is not possible to separate the recoils of different nuclei as shown in Fig. 7b. The cut applied on the energy deposit to get the projected beam profile (area/multiplicity > 1000) permits to remove the tritons in Fig. 7a and it is used for each studied energy domain. This cut ensures that the deposited energy is high enough so that the detector sees the particle from the beginning of the track to the end. The strip of the reaction is then well identified and the time of flight is calculated with less than 45 ns of accuracy in the argon mixture. Since the interaction can have taken place anywhere on the 1.6 mm wide strip, the spatial resolution is 0.46 mm rms.

Three different measurements of projected beam profile were made: the first with horizontal strips (vertical profile), the second with vertical strips (horizontal profile) and the third with the strips at 30° from horizontal. For example, Fig. 8 shows the profiles for the energy range of neutrons between 10 and 100 eV fitted by a Gaussian function.

The projected profiles were obtained from 10 eV to 20 MeV. Neutron energies below 10 eV could not be measured due to the memory limitation of the Acqiris digitizers (2 Msamples/strip), which prevented recording very long flight times. Above 20 MeV the analysis becomes more difficult since all the particle pulses begin to overlap and the contribution of pile-up events becomes important.

### 3.2.2. *Comparison with simulations*

The major difficulty in simulating geometries like the n_TOF facility is the large length

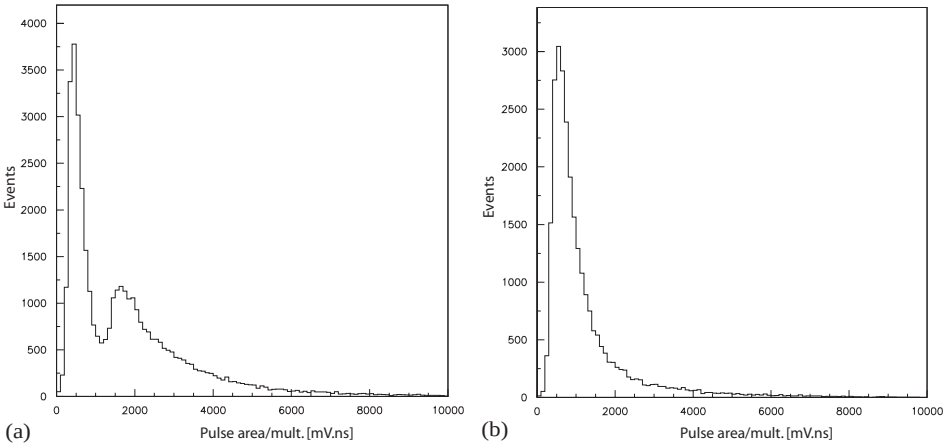


Fig. 7. Cluster area/multiplicity: (a) $E_n \in [10\ \text{eV}, 100\ \text{eV}]$, (b) $E_n \in [1\ \text{MeV}, 10\ \text{MeV}]$.

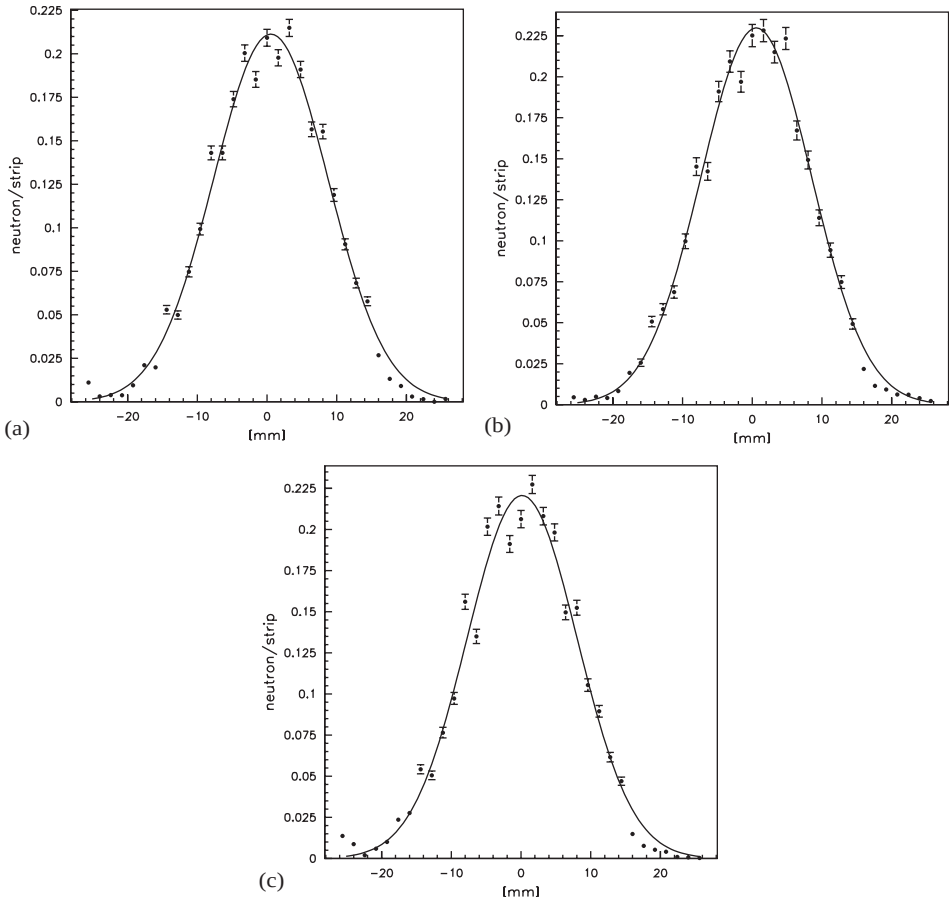


Fig. 8. Horizontal (a), vertical (b) and 30° (c) projected profiles between 10 and 100 eV at 186 m for one bunch of $7 \times 10^{12}$ protons, beam orientation.

($\sim$200 m) of the neutron flight path. The solid angle is so small that only one neutron out of $\sim 10^7$ emerging from the lead target will reach the detectors at the end of the neutron tube. Therefore, the strategy we followed for the beam profile simulation was to factorize the problem into two separate steps: (i) simulation of the spallation target and generation of the neutrons emerging from the aluminium window and entering in the neutron tube [15]; (ii) the geometrical transport of these neutrons through the neutron tube.

In the initial stage, two simulation codes were used, the intranuclear cascade code FLUKA [16] and the Energy Amplifier Monte Carlo code EAMC [17]. The detailed geometry of the lead spallation target and its surroundings were used as the input data. The code FLUKA was used for the production of fast neutrons with the spallation of 20 GeV protons onto a solid lead target, and the transport of the generated neutrons down to the cut-off energy of 19.6 MeV. The code EAMC was then used for the transport of neutrons with kinetic energy less than 19.6 MeV, where the neutron interaction databases were available. All the neutrons emerging from the lead target, through the aluminum window, with a direction lying inside a cone with a small aperture ($\theta < 10^\circ$) heading towards the experimental area, were recorded into a file.

In the second stage, the emerging neutrons were transported geometrically towards the detector through the neutron tube system. In this transport we assumed a perfect collimation system so that any particle touching the collimators or the tube was discarded. In order to enhance the statistics, we made the hypothesis that the direction of neutrons is isotropic within a small solid angle. Thus, each particle was reused several times by changing slightly its direction, in order to scan an area of a few cm$^2$ at the detector position. Each particle was weighted according to the number of times that it had been reused. The output histogram of this scanning gave us the 2D spatial distribution of the simulated neutrons arriving at the detector. The profiles have been projected with the same binning as real data for the three directions: horizontal, vertical and 30° (see Fig. 9).

After normalization, the maximum discrepancy between simulation and data is 20% in an energy region of low statistics (10–100 keV). This could have been due to different strip sensitivity, since some strips have more insulated spacers (to keep the width of the amplification gap) glued to them which changes their sensitivity. In the energy range 10–100 eV, this discrepancy is reduced to only 10% since the reaction rate is much bigger (Fig. 9). However, the shape of the different projections are in good overall agreement with the experimental results, consequently the simulation of the profile can be used for capture cross-section experiments.

### 3.3. Analytic approximation of the beam profile

It was possible to reconstruct a 2D beam profile shape $B(x, y)$ using the three different measurements we made with different orientations of the strips. This analytical approximation is of vital importance for cross section measurements since it provides information on the beam shape and on the number of neutrons received by the target as a function of their diameter and position.

The angle between the proton beam hitting the target and the n_TOF beam line is 10° and a small misalignment of the collimators is possible. This would have an effect on the centering and the orientation of the beam. Moreover, close to the collimator, the beam profile should show a plateau in its center. Thus, a correlated gaussian convoluted with a step function is chosen to fit the 2D beam profile, this function can fit the neutron beam profile anywhere after the second collimator:

$$B(x,y) \propto \frac{1}{2a}\left(\mathrm{Erf}(a + g(x,y)) - \mathrm{Erf}(g(x,y) - a)\right) \tag{4}$$

where

$$\mathrm{Erf}(u) = \frac{2}{\sqrt{\pi}} \int_0^u \mathrm{e}^{-t^2}\, \mathrm{d}t$$

and

$$g(x,y) = \sqrt{\frac{1}{2(1-\rho^2)}\left(\frac{(x-\mu_x)^2}{\sigma_x^2} + \frac{(y-\mu_y)^2}{\sigma_y^2} - 2{*}\rho\frac{(x-\mu_x)(y-\mu_y)}{\sigma_x\sigma_y}\right)}$$

$$B(x,y) = 0 \quad \text{for } r = \sqrt{(x-\mu_x)^2 + (y-\mu_y)^2} > R_{\max}$$

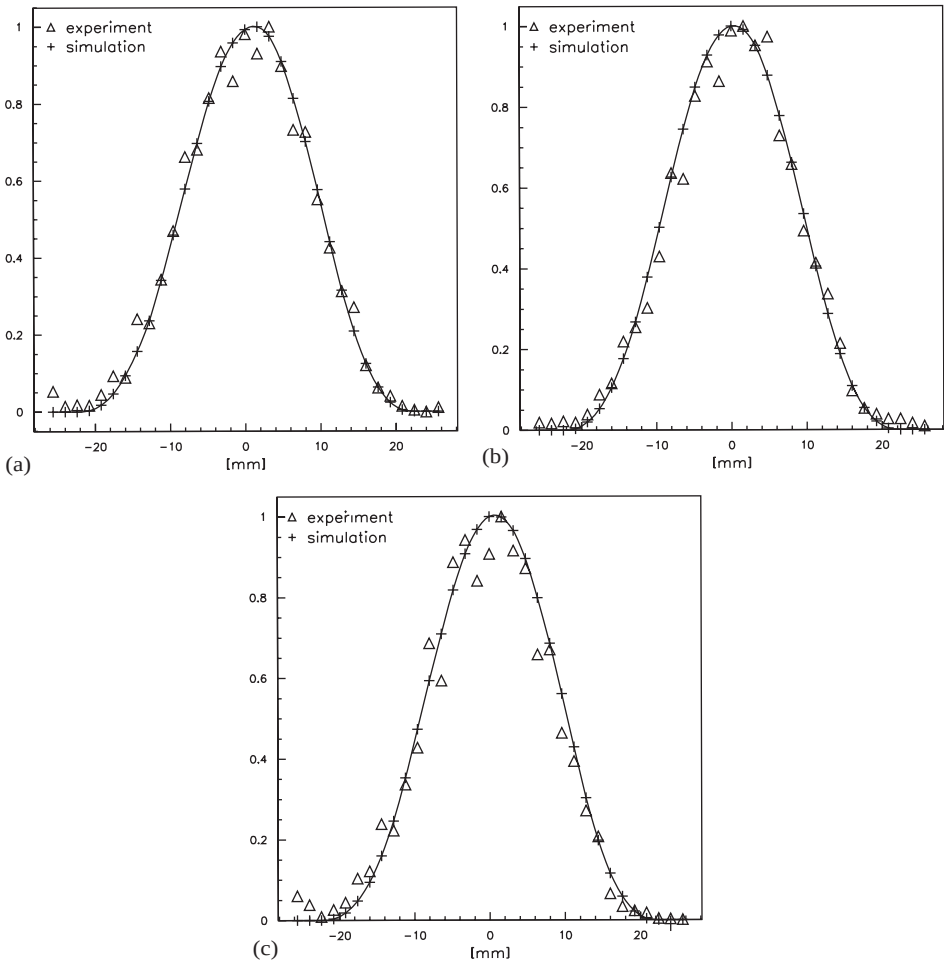


Fig. 9. Horizontal (a), vertical (b), 30° (c) experimental and simulated projected profiles between 10 and 100 eV at 186 m.

where $\mu_x$, $\mu_y$, $\sigma_x$, $\sigma_y$, $\rho$ and $a$ are free parameters. The parameter $a$ is a scale factor on the size of the step function, it is the parameter permitting to flatten the Gaussian in its center and fixing the size of the plateau.[3] The fitting function was put to zero for $r = R_{\max} > 21.5$ mm. It corresponds to the value at which the beam should be zero at 186 m as a consequence of the collimation system.

The neutron density detected in the strips of the detector is proportional to the integral of the beam intensity over the strips, so it is possible to adjust the free parameters and compare the integral of the $B(x, y)$ function over each strip with the values obtained experimentally. The integral of this function over each strip in the three different cases was calculated over a set of points $Q_{i,j}$ with $i \in \{1, 2..N = \text{strip number}\}$ and $j \in \{x, y, 30°\}$. The integration takes into account the exact length and width of the strips. The set of points $Q_{i,j}$ was compared to the experimental data $P_{i,j}$ with a $\chi^2$ [18]:

$$\chi^2 = \sum_{j \in \{x,y,30°\}} \sum_{i=1}^{N} \frac{(P_{i,j} - Q_{i,j})^2}{\varepsilon_{i,j}^2} \tag{5}$$

where $\varepsilon_{i,j}$ is the associated error to the experimental data $P_{i,j}$. It takes into account the

[3] The limit of the fitting function is a Gaussian when the parameter $a$ vanishes.

statistical error and the uncertainties due the detector and the number of protons. The total number of counts per proton bunch is calculated for each orientation ($x, y$ or 30°). The variation of this number gave an error estimated to 5% containing both the uncertainties due to the detector and on the number of protons. The code MINUIT [19] was finally used to adjust the free parameters of the function in order to minimise the $\chi^2$. The results of the fit are shown in Fig. 10 together with experimental data.

The values of the parameters adjusted to the experimental projected profiles at 186 m are reported in Table 2 with an upper energy limit of 20 MeV.

Table 3 shows the results of the fit for the simulated data. The main discrepancy between Tables 2 and 3 occurs in the 10 keV to 1 MeV energy range, and is mainly due to the poor statistics in this energy range caused by a lower reaction rate. This is also the reason why the errors on $\sigma_x$ and $\sigma_y$ are bigger in this energy range. The simulation agrees on the observed shift of the center on the $X$-axis, presumably due to the 10° angle of the proton beam on the target. However, the experimentally observed shift on experimental data of the center along the $Y$-axis was not foreseen, which implies a small but possible misalignment of the collimators or of the proton beam on the lead target. However, the general

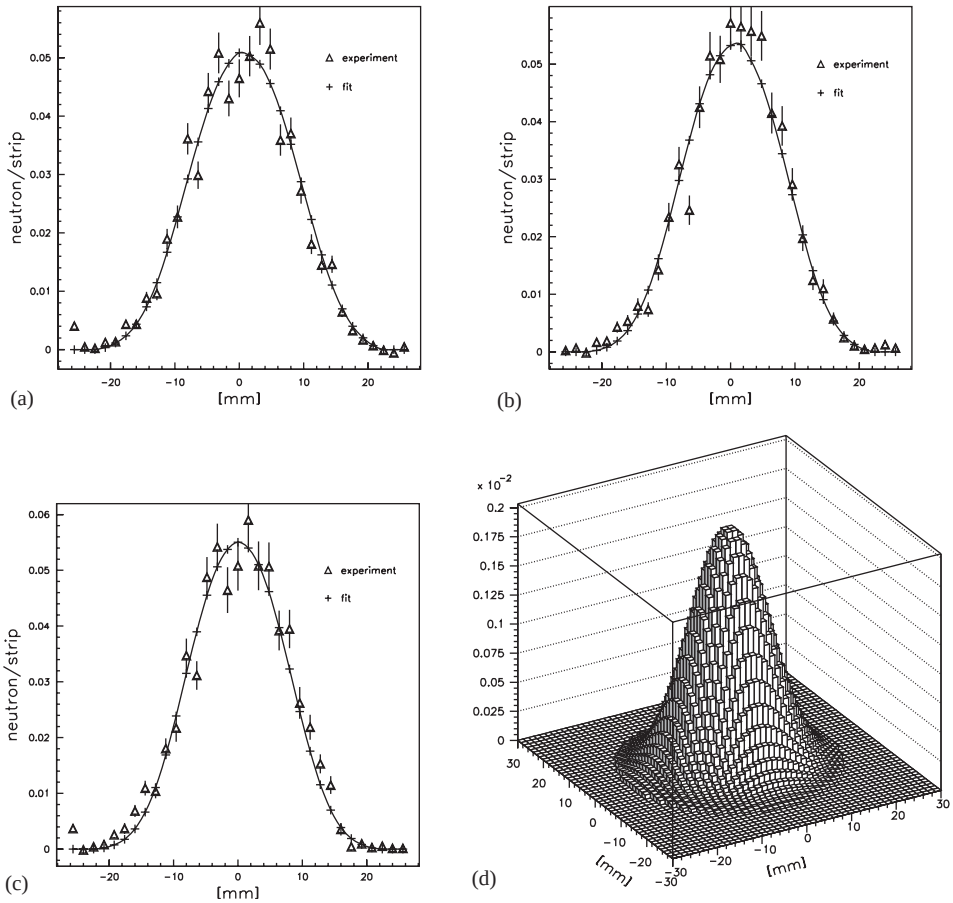


Fig. 10. Horizontal (a), vertical (b), 30° (c) experimental and analytic projected profiles between 100 keV and 1 MeV at 186 m and corresponding beam profile (d) for one bunch of $7 \times 10^{12}$ protons.

Table 2
Values of parameters $\mu_x$, $\mu_y$, $\sigma_x$, $\sigma_y$, $\rho$ and $a$ at 186 m by fitting experimental data

| Energy | $\sigma_x$ (mm) | $\sigma_y$ (mm) | $\mu_x$ (mm) | $\mu_y$ (mm) | $\rho$ | $a$ |
|---|---|---|---|---|---|---|
| 10 eV–100 eV | 5.6±0.1 | 5.4±0.1 | 0.41±0.01 | 0.21±0.01 | 0.01±0.02 | 1.33±0.01 |
| 100 eV–1 keV | 5.5±0.1 | 5.5±0.1 | 0.60±0.01 | 0.59±0.01 | 0.01±0.03 | 1.32±0.04 |
| 1 keV–10 keV | 5.8±0.1 | 5.9±0.2 | 0.8±0.1 | 0.5±0.1 | 0.05±0.05 | 1.25±0.03 |
| 10 keV–100 keV | 6.3±0.2 | 5.8±0.2 | 0.2±0.1 | 0.8±0.1 | −0.05±0.08 | 1.25±0.08 |
| 100 keV–1 MeV | 5.2±0.2 | 4.8±0.2 | 0.6±0.3 | 0.6±0.1 | 0.08±0.03 | 1.4±0.1 |
| 1 MeV–10 MeV | 4.6±0.1 | 4.3±0.1 | 1.2±0.1 | 2.3±0.1 | −0.03±0.02 | 1.40±0.04 |
| 10 MeV–20 MeV | 3.6±0.1 | 3.5±0.1 | 1.2±0.1 | 3.0±0.1 | 0.02±0.04 | 1.8±0.01 |

Table 3
Values of parameters $\mu_x$, $\mu_y$, $\sigma_x$, $\sigma_y$, $\rho$ and $a$ at 186 m by fitting the simulated data

| Energy | $\sigma_x$ (mm) | $\sigma_y$ (mm) | $\mu_x$ (mm) | $\mu_y$ (mm) | $\rho$ | $a$ |
|---|---|---|---|---|---|---|
| 10 eV–100 eV | 5.32±0.05 | 5.19±0.05 | 0.71±0.01 | 0.07±0.01 | 0.022±0.004 | 1.40±0.02 |
| 100 eV–1 keV | 5.33±0.05 | 5.29±0.05 | 0.61±0.01 | 0.04±0.01 | 0.02±0.01 | 1.35±0.01 |
| 1 keV–10 keV | 5.47±0.05 | 5.41±0.05 | 0.97±0.01 | 0.14±0.01 | −0.004±0.004 | 1.28±0.02 |
| 10 keV–100 keV | 5.31±0.04 | 5.25±0.04 | 0.82±0.01 | 0.18±0.01 | −0.005±0.003 | 1.31±0.01 |
| 100 keV–1 MeV | 5.20±0.01 | 5.13±0.01 | 0.90±0.01 | 0.10±0.01 | 0.003±0.001 | 1.34±0.05 |
| 1 MeV–10 MeV | 4.40±0.01 | 4.40±0.01 | 1.23±0.01 | 0.14±0.01 | 0.004±0.001 | 1.47±0.002 |
| 10 MeV–20 MeV | 3.38±0.05 | 3.37±0.04 | 1.29±0.01 | 0.22±0.01 | 0.018±0.008 | 1.88±0.04 |

Table 4
Values of parameters $\mu_x$, $\mu_y$, $\sigma_x$, $\sigma_y$ and $a$ at 185.2 m by fitting the simulated data

| Energy | $\sigma_x$ (mm) | $\sigma_y$ (mm) | $\mu_x$ (mm) | $\mu_y$ (mm) | $a$ |
|---|---|---|---|---|---|
| 10 eV–100 eV | 4.97±0.04 | 4.83±0.04 | 0.63±0.01 | 0.05±0.01 | 1.40±0.02 |
| 100 eV–1 keV | 4.95±0.04 | 4.92±0.04 | 0.54±0.01 | 0.04±0.01 | 1.40±0.02 |
| 1 keV–10 keV | 5.09±0.04 | 5.05±0.04 | 0.86±0.01 | 0.13±0.01 | 1.32±0.02 |
| 10 keV–100 keV | 4.99±0.03 | 4.93±0.03 | 0.80±0.01 | 0.17±0.01 | 1.35±0.01 |
| 100 keV–1 MeV | 4.87±0.01 | 4.83±0.01 | 0.79±0.01 | 0.07±0.01 | 1.37±0.01 |
| 1 MeV–10 MeV | 4.06±0.01 | 4.05±0.01 | 1.10±0.01 | 0.13±0.01 | 1.58±0.001 |
| 10 MeV–20 MeV | 3.14±0.04 | 3.13±0.04 | 1.27±0.02 | 0.20±0.02 | 2.02±0.04 |

agreement on the parameters fitted from simulation and experiment confirms the validity of the simulation.

### 3.4. *The beam profile at* 185.2 *m*

The targets of interest for the neutron induced cross section measurement are placed inside a sample changer at 185.2 m. Table 4 gives the result of the fit on the simulated data at this particular location and the value of the parameters are shown in Fig. 11. The correlation coefficient $\rho$ has been fixed to 0. This result is interesting for the evaluation of the cross-sections as it permits the calculation of the fraction of the beam seen by the sample usually smaller than the beam (typically 19% for a 10 mm diameter sample). Futhermore the error induced by a possible misalignment of the sample in the beam can be propagated and transcribed in an error on the flux fraction and then on the cross-sections.

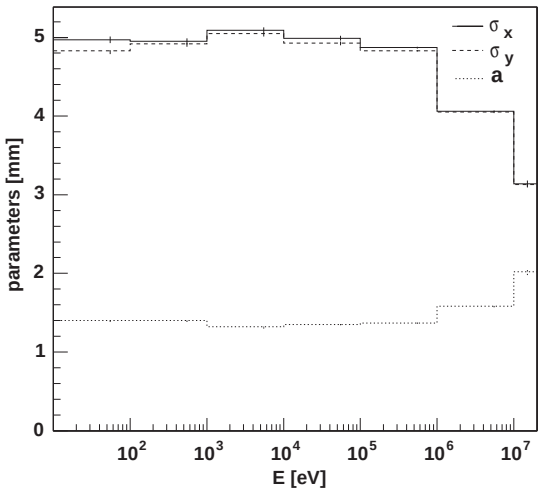


Fig. 11. The values of $\sigma_x$, $\sigma_y$ and $a$ (parameter with no dimension) with an uncorrelated gaussian as a function of the neutron energy.

## 4. Conclusion

Measurements of the spatial characteristics of the n_TOF neutron beam have been performed with the Micromegas detector. The use of signals from both the $^6$Li$(n,\alpha)$t reaction and the recoils in the detector gas permits to measure accurately the shape of the beam profile over a wide energy range. The n_TOF beam profile was also fitted by an analytic function and compared to simulations from 10 eV to 20 MeV. The knowledge of the beam profile is crucial for the measurement of neutron capture cross-sections. In the future we plan to improve Micromegas based neutron detection by including a two-dimensional read out. This new type of neutron detector could have some important applications in medical engineering (characterization of neutron beam) and in neutron tomography.

## Acknowledgements

We would like to thank D. Barbas and E. Virassamynaiken from the CENBG in Bordeaux (France), and D. Damianoglou and T. Klados from the university of Thessaloniki in Greece for their help for the construction of the detector.

## References

[1] C. Rubbia, et al., CERN/LHC/98-02 (EET) and CERN/LHC/98-02 (EET)-Add, CERN, Geneva, Switzerland.
[2] C. Borcea, et al., Nucl. Instr. and Meth. A 513 (2003) 524.
[3] C. Rubbia, et al., CERN/AT/95-44(ET), CERN, Geneva, Switzerland.
[4] S. Andriamonje, et al., Phys. Lett. B 348 (1995) 697.
[5] H. Arnould, et al., Phys. Lett. B 458 (1999) 167.
[6] G. Charpak, et al., CERN LHC/97-08(EET), CERN, Geneva, Switzerland.
[7] Y. Giomataris, Nucl. Instr. and Meth. A 419 (1998) 239.
[8] Y. Giomataris, Ph. Rebourgeard, J.P. Robert, G. Charpak, Nucl. Instr. and Meth. A 376 (1996) 29.
[9] The n_TOF Collaboration. n_TOF Technical Report. CERN/INTC 2000-018, CERN, Geneva, Switzerland.
[10] S. Andriamonje, et al., Nucl. Instr. and Meth. A 481 (2002) 120.
[11] Gleen F. Knoll, Radiation Detection and Measurement, 2nd Edition, Wisley, New York, 1989.
[12] H. Wendler, E. Schaefer, P. Betev, P. Pavlopoulos, R. Plag, V. Ketlerov, in preparation.
[13] http://www.srim.org
[14] Cross Section Evaluation Working group, Data format and procedures for the evaluated nuclear data file ENDF-6, National Nuclear Data Center at BNL, 2001.
[15] V. Vlachoudis, et al., CERN/SL-NOTE-2000-029 EET, CERN, Geneva, Switzerland.
[16] A. Fasso, et al., Proceedings of a Specialist Meeting, Issy Les Moulineaux (France), Intermediate Energy Nuclear Data: Models and Codes, 30 May–1 June 1994, OECD, p. 271.
[17] F. Carminati, et al., CERN/LHC/EET 1996-011, CERN, Geneva, Switzerland.
[18] W.H. Press, et al., Numerical Recipes in C, 2nd Edition, Cambridge University Press, Cambridge, 1992.
[19] F. James, MINUIT: Function Minimization and Error Analysis, CERN, Geneva, 1994.